[type=editor, auid=000,bioid=1,orcid=0000-0000-0000-0000]

Highlights

Investigation of Nutrient Cycling and Speed-Based Biomass Decay in the Hyporheic Zone

Marc Berghouse, Rishi Parashar

- Research highlight 1
- Research highlight 2

Investigation of Nutrient Cycling and Speed-Based Biomass Decay in the Hyporheic Zone

Marc Berghouse[a,b], Rishi Parashar[b]

[a] *University of Nevada, Reno*
[b] *Desert Research Institute*

Abstract

Within the hyporheic zone, a complex interplay of abiotic processes dictates the growth conditions of biomass. Given the hyporheic zone's potential role to bioremediate contaminants through biotic and abiotic reduction, decoding these growth determinants has broader ecological significance. In this study, we present a Monte-Carlo-style exploration into how varied initial conditions influence biomass growth. Our modeling approach simulates a two-dimensional, meter scale cross-section of the hyporheic zone, integrating heterogeneous permeabilities and accurate hyporheic flux, and modeling chromium reduction through Monod kinetics.

To effectively capture bioclogging dynamics and soil respiration, we've enhanced the reactive transport model, PFLOTRAN. Our expanded model accounts for biomass decay influenced by fluid velocity, and the dependency of biomass growth on temperature. We highlight the impacts of our velocity-based biomass decay function by providing a sensitivity analysis of the impact of different parameter values on biomass growth and chromium reduction. In addition, we generate 375 variations of simulations to offer holistic insights into microbial growth dynamics through mean trend analysis, mean spatial distribution analysis, sensitivity analysis, PCA and clustering, and correlation heatmaps. This analysis reveals a number of unreported phenomena, and shows that abiotic reduction is more dominant than biotic reduction, even in cases of high biomass concentrations. In this study, we thus contribute theoretical model developments for biomass growth in saturated porous environments, a working version of our biomass growth model in PFLOTRAN, and analysis of the feedback cycles and variable relationships present in our simulations.

Keywords:

1. Introduction

Historically, studies in the HZ have primarily revolved around understanding flow dynamics [1, 2, 3], nutrient flux [4, 5, 6], and biofilm growth [7, 8, 9, 10]. (Couple sentences on flow dynamics and nutrient flux research). Most of the current research on biomass growth in the HZ relates to the ecological significance of microbial communities [11, 12, 13, 14], but recent research has also illuminated the impact of biofilms on physical hydrologic properties such as permeability and local flow speed [9, 10, 15, 16]. Specifically, the emergence of biofilms, which causes a decrease in permeability known as bioclogging, has been recognized as a significant factor affecting water flow and solute transport [7, 17, 18]. Furthermore, variations in the properties of biofilms such as strength, density and stickiness, and variations in the geometry of the porous media such as grain shape, impact the relative changes in permeability [17]. The degree of bioclogging is also dependent on flow speed. As speed increases, the increased fluid shear causes a breakup of the biofilm which represents a local decrease in biomass concentration.

Biomass growth in the hyporheic zone can be understood as a complex feedback loop dependent on a myriad of individual phenomena. Flow, as an initial causal variable in most cases, acts as the foundation for this feedback loop. It instigates a flux of temperatures and nutrient concentrations within the hyporheic zone. This flux, in turn, triggers changes in biomass concentrations. Generally, higher nutrient levels and increased temperatures tend to promote growth [19, 20, 21, 22]. However, the relationship between temperature and biomass is somewhat nuanced. For instance, an uptick in temperature leads to reduced water viscosity, which subsequently results in increased flow speeds. Increased fluid speed may bring in nutrient-rich or nutrient-poor water, resulting in changes to the biomass growth within the domain. Furthermore, high shear rates caused by increased fluid speed can result in the breaking apart and subsequent transport of biomass. However, the coupling of these multiple phenomena has not yet been investigated, meaning the exact impact of temperature on biomass growth in the hyporheic zone is not fully understood.

Biomass growth can also influence a soil's permeability [23, 24]. As biofilms become denser, they lead to bioclogging, reducing soil permeability. This impedes the nutrient dispersion across the hyporheic zone, subsequently

slowing biomass growth. This dynamic between biomass and permeability creates a negative feedback loop within the overarching feedback mechanisms. More biomass leads to reduced permeability, which in turn diminishes biomass growth. Many studies have investigated how bioclogging alters permeability (cute), but few studies have simulated the impacts of permeability on biomass growth (cite). Furthermore, bioclogging simulations are often done in the context of homogeneous permeability simulations, meaning the impacts of soil heterogeneity on bioclogging and biomass growth are not well understood.

Reactive transport (RT) simulators [25, 26, 27] have emerged as powerful tools that allow for investigation and prediction of phenomena within the hyporheic zone [28, 29, 30, 31]. Field and lab studies are often resource-intensive and require a large amount of time. Although not able to capture the same novelty and richness of information available from in-situ measurements, RT simulations offer a highly analytical viewpoint of known physical and chemical phenomena that can be accurately described through systems of equations. RT simulators are constantly being updated to include newly understood interactions. However, given their vast complexities, it is inevitable that there will always be new relevant models that have yet to be applied to RT simulators, such as the velocity-based decay of biofilms.

In this paper, we aim to provide two major contributions. First, we seek to further our understanding of the hyporheic zone by investigating the complex relationships governing biomass growth for a variety of input conditions. Furthemore, we highlight the nuanced relationships between abiotic elements and bacterial proliferation and highlight how these relationships impact chromium reduction in the hyporheic zone. Second, we seek to highlight the sensitivity of our velocity-based biomass decay in terms of biomass growth and chromium reduction.

2. Methods

2.1. Description of RT Simulations

2.1.1. Description of Chrotran

Our simulations are built upon PFLOTRAN [26], a sophisticated multiphysics reactive transport simulator developed collaboratively by multiple national laboratories. Specifically, we have adapted the Chrotran [32] version of PFLOTRAN to create a high-complexity simulation of biomass growth in the hyporheic zone at the Darcy scale. Chrotran models the dynamics of

five key species: a heavy metal contaminant (in our case, Cr(VI)), an electron donor, biomass, a non-toxic conservative bio-inhibitor, and a biocide. It incorporates both direct abiotic reduction through donor-metal interaction and biotic reduction driven by donor-induced biomass growth. Chrotran uses Monod kinetics to define biomass growth as a function of electron donor concentration, with additional factors accounting for biomass crowding, inhibition and decay. We chose to make the input concentrations of bio-inhibitor and biocide low to simplify the analysis of our simulations. Chrotran also includes crucial processes such as donor sorption (through a mobile-immobile mass transfer system), bio-fouling, and biomass death. Furthermore, Chrotran allows for bioclogging modeling by dynamically updating porosity and hydraulic conductivity based on biomass concentration. The software can handle heterogeneous flow fields and arbitrarily many chemical species and amendment injection points, featuring full coupling between flow and reactive transport. For a comprehensive description of Chrotran's capabilities and mathematical formulation, please refer to their paper [32].

2.1.2. Velocity-Based Biomass Decay

We made initial modifications to the published version of Chrotran by adjusting its parameters. Specifically, we calibrated biomass growth rates to align with the limited data available on biomass growth in the hyporheic zone [33, 34, 35]. Additionally, we adjusted steady-state concentrations to be broadly representative of those found in wetland environments [36].

The original Chrotran model defines biomass decay using a simple linear function that only considers the current biomass amount and a minimum biomass threshold. However, recent research suggests that biomass decay can also be influenced by shear stress [17]. Specifically, research has shown that the thickness of biofilms has an inverse logarithmic relationship with shear stress. In our study, we consider biofilm and biomass to be interchangeable. At high flow velocities, significant shear stresses can form at permeability boundaries, potentially dislodging and transporting biofilms and bacterial deposits. While ideally, we would incorporate shear stress values directly into Chrotran's biomass decay function, PFLOTRAN lacks the capability to calculate these stresses. As an alternative, we developed a function that calculates cell-specific biomass decay based on cell-specific Darcy velocity (equation 1).

$$\lambda_b = \lambda_{B2}(v - \alpha)^{\beta(B-B_0)} \tag{1}$$

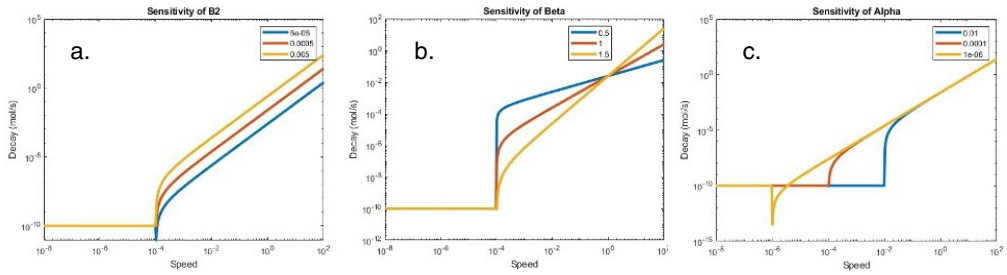

Figure 1: Sensitivity analysis of parameters in the augmented biomass decay equation. (a) Sensitivity of the B2 parameter. Higher values of B2 result in a larger amount of initial decay for speed>1e-4, but don't impact the long-term slope of the relationship between speed and decay. (b) Sensitivity of the Beta parameter. Higher values of Beta result in a smaller amount of initial decay but a greater slope. (c) Sensitivity of the Alpha parameter. Higher values of alpha result in a greater increase in initial decay, but the speed required to produce the initial decay is greater.

B2 represents the background decay rate based on environmental factors. B is the concentration of biomass (mol/m^3), and B0 is the initial, or background, biomass concentration. V represents the Darcy velocity of the fluid. Alpha is a fitting parameter that physically represents the fluid speed required to start the shearing of biomass. Beta is a fitting parameter that represents the rate of increase of decay as flow speed increases. For low values of beta, low flow speeds will cause a small increase in biomass decay, and high flow speeds will cause a medium increase in biomass decay. For high values of beta, low flow speeds will have essentially no impact on biomass decay, but high flow speeds will cause a large increase in biomass decay. Thus, beta represents both the speed required to cause a significant increase in biomass decay and also the rate that biomass decay increases at as flow speed increases. We can see from the sensitivity analysis of this equation (Fig. 1) that the amount of decay is 1e-10 below a speed of about 1e-4 (depending on the value of alpha). For our implementation in PFLOTRAN, we use a conditional statement that returns the value of $(v - \alpha)$ if $v > \alpha$, else we return 1e-10 in place of $(v - \alpha)$.

The underlying premise of our biomass decay equation is that initial scouring establishes a steady-state biomass concentration at a given flow velocity. Subsequent increases in flow velocity lead to enhanced scouring, attributed to both the elevated flow speed and the formation of preferential flow channels within the biofilm matrix. We calibrated the fitting parameters α

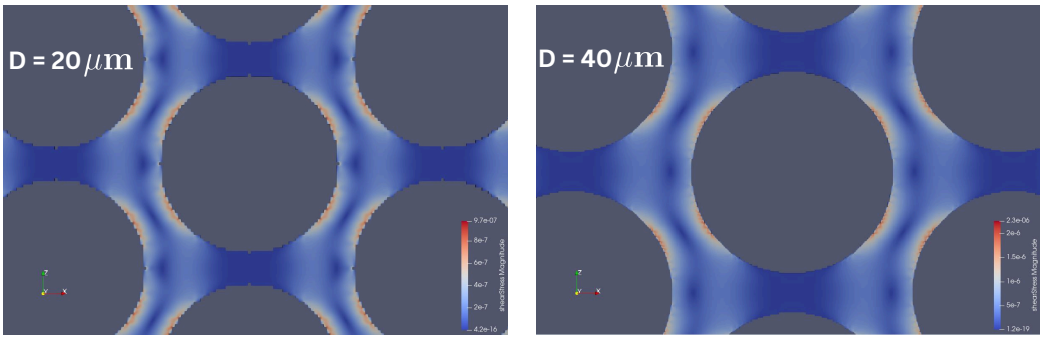

Figure 2: Shear stress fields derived from OpenFoam simulations of a 25% porosity geometry with a grain diameter of 20 μm and 40 μm. The D=20 μm simulation has a mean shear stress of 1.27e-7 and a max shear stress of 7.89e-7. The D=40 μm simulation has a mean shear stress of 2.71e-7 and a max shear stress of 1.86e-6. The ratio of max to mean shear stress increases as grain diameter increases (6.21 to 6.86), indicating that a pore scale correction factor of 10 is reasonable for our simulations, where average grain diameters may theoretically range from less than 1 μm (clay) to 100mm (gravel).

and β through a comparative sensitivity analysis with published research on biofilm thickness as a function of shear stress [17]. It is well-established that the distribution of micro- and pore-scale velocities can diverge significantly from Darcy-scale velocities [37]. Given that biofilms primarily develop within pore spaces, they are subject to pore-scale velocity variations, resulting in higher shear stresses on the biofilms compared to Darcy-scale calculations. To address this scale discrepancy, we employed OpenFOAM [38, 39] to simulate two homogeneous porous geometries, each measuring 665 μm by 665 μm, with a porosity of 25% but differing in pore length and grain diameter (Fig. 2). Both simulations revealed an approximate order of magnitude difference between mean and maximum shear stresses. Consequently, we applied a pore-scale correction factor of 10 to adjust the shear stresses derived from PFLOTRAN's Darcy-scale simulations.

In our shear stress calculations from PFLOTRAN, we opted to use the maximum shear stress rather than the average. This decision is justified by the sparse spatial distribution of significant shear stresses, which primarily occur at interfaces between units of differing permeability where large velocity gradients exist (Fig. 3). While our Gaussian permeability fields contain few sharp discontinuities, real soil systems typically exhibit high heterogeneity at the pore scale, suggesting that our simulated shear stress fields are likely more uniform than reality. Therefore, we posit that the maximum shear

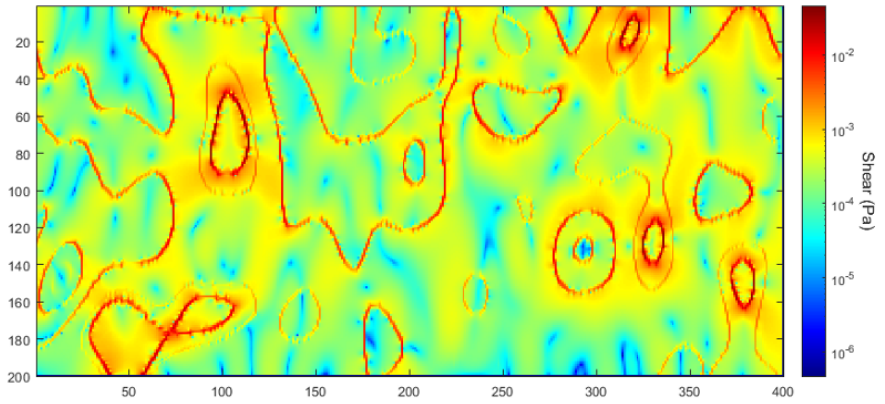

Figure 3: Average shear stress field for the high-speed calibration simulation. High shear values (5e-3 to 5.4e-2), indicated by red color, occur due to sharp transitions in permeability and high velocity magnitude. The top right section of the domain contains preferential channels with high local velocities. When these high velocities encounter low-permeability transitions, their directions change and velocities significantly reduce, resulting in large velocity gradients (and thereby shear magnitudes). Areas of the spatial domain with lower velocity or less transitions between high and low permeability, which comprise the majority of the total area, generally have shear values of 1e-5 to 6e-4.

stress serves as a reasonable proxy for the true mean shear stress in more heterogeneous systems.

To validate our approach, we created three baseline simulations and calculated their shear stresses using the aforementioned methodology. We then correlated these values with those presented in Figure 5 of [17], computing the percentage difference in biomass concentrations for each increment in shear stress (Fig. 4). These percentage differences were compared to the corresponding changes in biomass thickness reported in the literature, allowing for a final calibration. This comprehensive calibration process yielded optimal values of $\beta = 0.8$ and $\alpha = 2 \times 10^{-7}$. This rigorous approach to parameterization, incorporating both theoretical considerations and empirical data, enhances the robustness and applicability of our biomass decay model across various hydrodynamic conditions in the hyporheic zone.

In addition to our augmentation of the biomass decay equation, we also altered the standard Chrotran biomass growth function to depend on temperature. Numerous studies have shown that microbial growth generally increases with increasing temperature [40, 41, 42, 43],. To include this de-

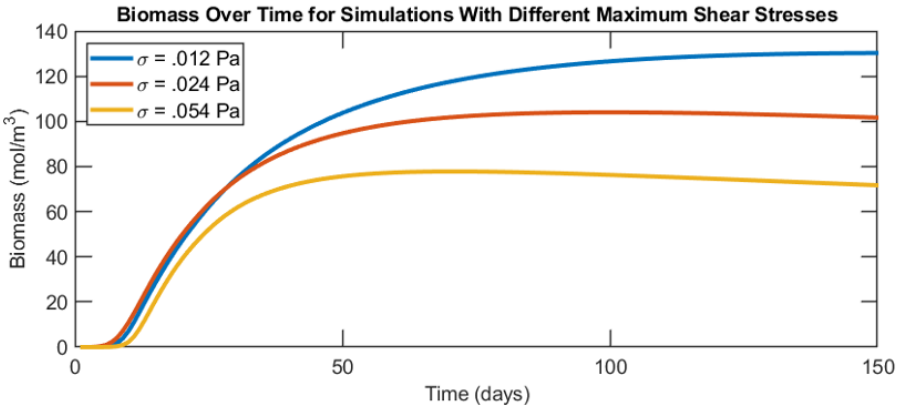

Figure 4: Biomass time series for a low-speed (blue), medium-speed (orange), and high speed (yellow) simulation. The legend gives the maximum shear for each simulation. With the pore-scale to darcy-scale correction of 10, we get max shear values of .054, .024, and .012. From the paper, these shear values correspond to biofilm thicknesses (after a 14 hour growth period) of 18, 25 and 31, or a 19% decrease in thickness going from sigma = .012 Pa to sigma = .024 Pa and and 28% decrease in thickness going from sigma = .024 Pa to sigma = .054 Pa. Our steady-state biomass concentrations show similar percentage differences (22% and 29%), indicating a relatively accurate calibration of our velocity-based biomass decay.

pendency in PFLOTRAN, we parameterized the Ratkowski function [44] as

$$\lambda_{B_T} = P_1 T^6 + P_2 T^5 + P_3 T^4 + P_4 T^3 + P_5 T^2 + P_6 T + P_7 \tag{2}$$

where $P_1 = -2.9 \times 10^{-9}$, $P_2 = 2.3 \times 10^{-7}$, $P_3 = -6.5 \times 10^{-6}$, $P_4 = 6 \times 10^{-5}$, $P_5 = 1.4 \times 10^{-4}$, $P_6 = 2.4 \times 10^{-2}$, and $P_7 = 0.196$. Plugging this into the original Chrotran biomass growth equation gives us

$$\mu_b = \lambda_{B1} \lambda_{B_T} B \frac{D}{K_D + D} \left(\frac{K_B}{K_B + B}\right)^{\alpha} \tag{3}$$

2.1.3. Permeability and Flow

Studies have shown that biomass growth in the hyporheic zone is strongly linked to the hyporheic flux [9, 7, 45, 46]. Depending on the concentration of nutrients and the flow speed of the groundwater and surface water flows, a positive or negative flux can have different impacts on growth. To gain deeper insight into how exactly these differences affect biomass growth, we simulated the hyporheic zone under a variety of realistic flow conditions (Fig.

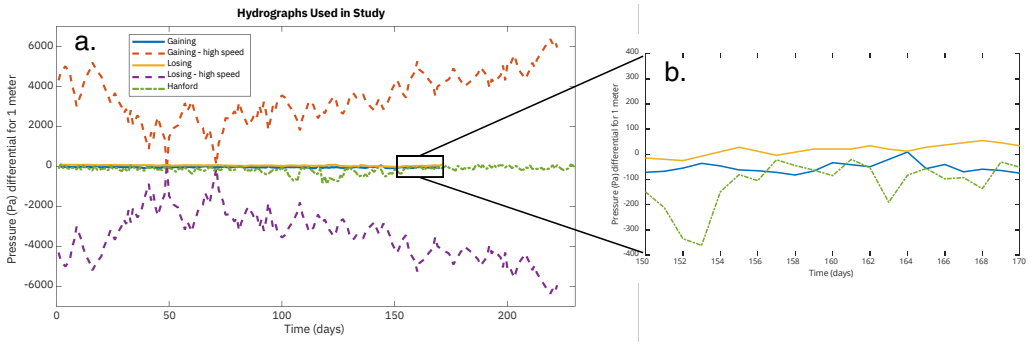

Figure 5: Time-series of pressure boundary condition groups used in the simulations. For each group, slight variations to the time-series were introduced to develop a much wider variety of potential flow conditions for the simulations.

5a). The gaining and losing flow conditions at high speed represent the largest hyporheic fluxes we were able to find in the literature (cite), the low-speed gaining and losing conditions represent much smaller fluxes, and the medium-speed conditions are an average between the low-speed and high-speed conditions. In addition, we use hydrographs that come from hyporheic flux data measured at the Hanford site (cite). Thus, we examine feedback cycles and statistical relationships in the hyporheic zone from a general perspective that can be considered the average of a variety of previously published data.

In addition to the general direction and magnitude of flow, permeability has a significant influence on the general transport of nutrients and biomass within the hyporheic zone. At low permeabilities, biomass and nutrients are less able to disperse throughout the hyporheic zone, so average biomass concentrations over a large area will be less. However, hotspots of high biomass concentration may still form in low permeability zones, which may also result in bioclogging. To understand how exactly biomass growth is impacted by a variety of permeabilities, we created a variety of heterogeneous permeability fields with different covariance ratios (Fig. 6). Although the mean permeability was similar for most simulations (around 2e-10 m2), the effective permeability (Keff) would change based on the covariance ratio. Furthermore, we also ran simulations at extremely low permeability to understand biomass growth in a significantly different environment.

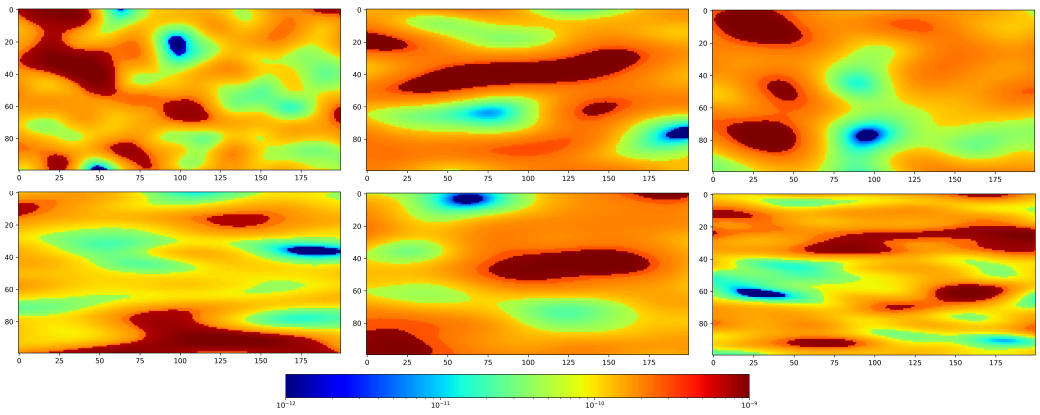

Figure 6: Sample heterogeneous permeability distributions (at t=0) used in simulations featured in this study. This figure is also featured in some of our unpublished work on upscaling the simulations discussed in this study.

2.1.4. Boundary Conditions

We model a segment of the hyporheic zone as a vertical slice measuring 1 meter in height and 2 meters in length. This slice represents the interface between groundwater and surface water, with the top and bottom boundaries corresponding to surface flow and groundwater respectively. The left and right boundaries extend the hyporheic zone longitudinally along the direction of river or groundwater flow. Flow conditions at the top and bottom are controlled by Dirichlet boundaries, with pressure differentials set according to the simulation type: gaining, losing, or hanford. The lateral boundaries allow for bidirectional flow seepage, regulated by a Dirichlet pressure boundary of zero. Transport boundary conditions mirror those used for flow. A variety of scales were used for the simulations in our study. For our analysis of feedback cycles and general relationships observed in our simulations, we created simulations that were 1x2 meters, 1x4 meters, and 1x20 meters that all had a dx and dy of 0.01 meters. For our sensitivity analysis of the impacts of our velocity-based biomass decay on biomass growth and chromium reduction, we created simulations that were 1x2 meters and had a dx and dy of 0.005 meters.

2.1.5. Simulation Variables

The variables (also referred to in this work as features) of the simulations, as well as their range of possible values, are given in Table 1. All of the features that depend on the time-evolution of the simulation, such as biomass,

Table 1: Description of physio-chemical features and their ranges of possible values used in the simulations. B: biomass, ED: electron donor (molasses), Cr: chromium, V: velocity, P: pressure, T: temperature, ϕ: porosity, k: permeability.

Var	B ($\frac{mol}{m^3}$)	ED ($\frac{mol}{L}$)	Cr(VI) ($\frac{mol}{L}$)	V_y ($\frac{m}{hr}$)	V_x ($\frac{m}{hr}$)	P (Pa)	T ($^\circ C$)	ϕ	k (m^2)
Min	1e-10	1e-20	1e-20	-632	-486	-1214	4.8	1e-4	1e-15
Max	765	5.5e-3	7.6e-3	671	651	7099	25	0.6	1e-9
Mean	58	8.1e-6	1.4e-5	-5.8e-2	-1.4e-2	786	11.5	0.13	2e-10

chemistry, and flow speed, are referred to as the "physio-chemical features". The variables that are prescribed at the beginning of the simulation and don't change value over time are referred to as "input variables".

2.2. Sensitivity Analysis

One of the primary goals of this study is to gain deeper insight on the abiotic controls of biomass growth in the hyporheic zone. To this extent, we employ a variety of sensitivity and correlation analyses to understand how different features may impact growth. We use classical sensitivity analysis, changing one feature and keeping all others equal, to determine the individual impacts that each feature may have on biomass growth. Furthermore, we use a Monte-Carlo-type sensitivity analysis to understand feature relationships at a more global level. Specifically, we ran 375 simulations of the hyporheic zone, each under slightly different input conditions, then used PCA and cluster analysis to understand physio-chemical feature relationships and groupings. In addition, we used a correlation heatmap to identify correlations between all the simulation features (both physio-chemical features and input variables).

3. Results and Discussion

3.1. Feedback and Mechanisms of Biomass Growth

The primary known physio-chemical features that impact biomass growth at scale, as well as their general relationships with each other, are shown in Figure 7. While modeling of oxygen concentrations was beyond the scope of this study, we included it as a primary variable in the biomass feedback loop because of the vast literature detailing the impacts of oxygen depletion on bacteria [45, 47, 48]. Furthermore, each of these physio-chemical features and relationships have previously been reported on in the literature (cite). These interactions were also discussed in the introduction, but essentially,

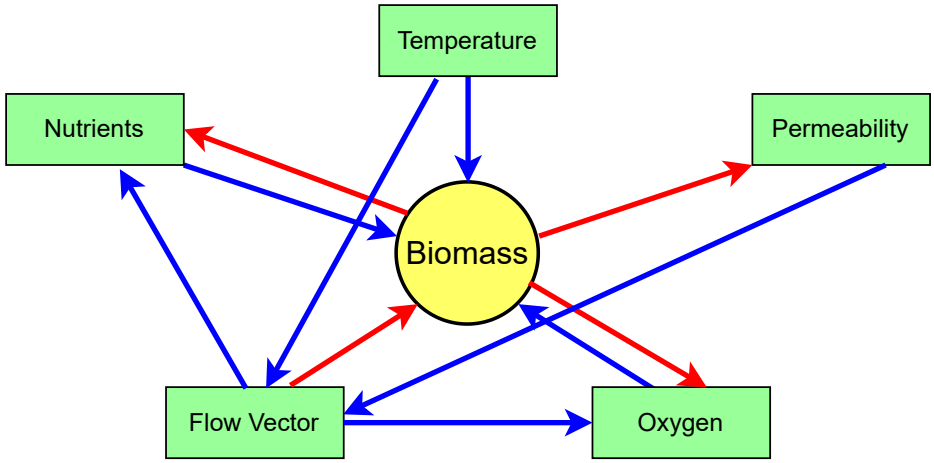

Figure 7: Known feedback cycles from physical features present in simulations of biomass growth in the hyporheic zone. A blue arrow signifies a positive causative effect (increase leads to increase), and a red arrow indicates a negative causative effect (increase leads to decrease).

changes in flow cause changes in nutrient concentrations and temperature which then cause changes in biomass growth. As biomass grows, it consumes nutrients and oxygen, and reduces the local permeability of its substrate. This decrease in permeability in turn causes a decrease in local fluid speed.

The only new connection that our study adds, that, although previously known, had not yet been incorporated into reactive transport models, is speed-based biomass decay. We should also note here that these represent the primary intuitive relationships most important for biomass growth, but don't necessarily reflect the results of our own simulations. In our own simulations, which are further discussed in greater detail throughout the rest of the paper, we find temperature to have a small negative correlation with biomass, and we find pressure to have a greater correlation with biomass than either of the velocity components. (at the end, make another figure 7 with adapted relationships?).

The average spatial distributions of the physio-chemical features for one of our losing simulations (Fig. 8) can be used to elucidate some of the relationships in our biomass growth feedback loop. Biomass is greatest in the high-porosity zones around the edges of the domain, and concentrations are smallest in the low-porosity zone in the middle of the domain. Where fluid

speeds are largest, we see the greatest amount of lateral extension of biomass towards the middle of the domain. In addition, a small amount of velocity-based biomass decay can be observed in the lower right corner of the domain for the biomass distribution. The spatial distribution of molasses looks similar to that of biomass except the gradients are smoother. The temperature and Cr(VI) distributions are primarily determined by the horizontal flow (V_y). Because pressure is lowest at the bottom boundary, a left-to-right pressure gradient exists near the left boundary, causing a rightward flux of fluid. The right boundary has the greatest pressure in the domain, meaning that flow is generally right to left in this simulation (negative V_y). Thus, the high Cr(VI) concentrations are a result of inward flux from the left side of the domain, and the low Cr(VI) concentrations are a result of inward flux from the right side of the domain. The impacts of biomass growth on Cr(VI) reduction can be seen in the slightly elevated concentrations of Cr(VI) near the right boundary where biomass concentrations are high. Although molasses concentrations are also high here, most of it is immediately consumed by biomass and won't be available for abiotic reduction. Thus, where biomass concentrations are lower, even though molasses is also lower, we see greater reduction in chromium concentrations, in other words, the scale of the variability of biomass concentrations (x=400 to x=350 is a 200 times increase in concentration) is greater than that of molasses concentrations (x=400 to x=350 is a 7 times increase). Because of this difference in scales, between x=300 and x=350 abitiotic reduction dominates and chromium concentrations are lower than they are where biomass is high.

In addition to the average spatial distributions of key physio-chemical features for a single time series, we present the average normalized spatial distributions of the physio-chemical features over all of our simulations (Fig. 9). This figure represents the general spatial trends that persist after averaging over each 1x2 meter simulation. The averaged spatial distributions of biomass, molasses (labeled as ED in Figure 9) and Cr(VI) all have a significant degree of similarity due to the boundary conditions of the simulations. Although the concentrations of these features were randomized in our simulations, the predominant direction of flow over the entirety of our simulations is from top (surface water) to bottom (groundwater). However, the surface water contains decreased levels of ED relative to the groundwater, meaning biomass growth is generally greater in the gaining simulations. Thus, as groundwater flows into the domain from the bottom, and because nutrient and biomass concentrations had low initial values and the transport condi-

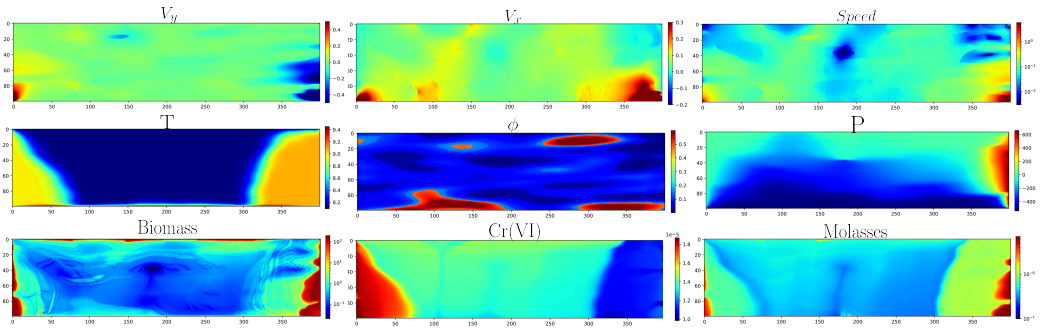

Figure 8: General (averaged over all simulations and time steps) trends for key physio-chemical features. Each variable is normalized, with 0 (dark blue) corresponding to low values and 1 (dark red) corresponding to high values.

tions are greater than those at the top boundary, each of these variables shows high values near the bottom of the domain. The high concentrations of biomass on the right side of the domain are entirely a result of the fact that most simulations featured lateral flow moving from the right to left side of the domain. Porosity, although impactful at the level of a single simulation, seems to have no impact on biomass or ED concentrations when averaged over all simulations. However, porosity does have a large impact on immobile molasses concentrations, with higher amounts of ED_{im} appearing where porosity is high. Similar to the average spatial distributions for a single simulation, the average spatial distributions over all simulations show the impacts of fluid speed on biomass decay as a slightly lower concentration of biomass in the lower right corner.

These results highlight the complex interplay between physical, chemical, and biological processes in the HZ, demonstrating the importance of considering spatial heterogeneity and temporal dynamics in modeling efforts. The observed dominance of abiotic reduction over biotic reduction, even in areas of high biomass concentration, challenges conventional assumptions and has significant implications for bioremediation strategies.

3.2. General Trends

The general trends of the physio-chemical features are shown through their mean feature plots (Fig. 10). The red dotted lines in each time series plot show the time value of the inflection points for biomass growth (Fig. 10e). Average biomass concentrations increase very slowly for the first 18 days, increase rapidly for the next 36 days, then increase at a lower growth

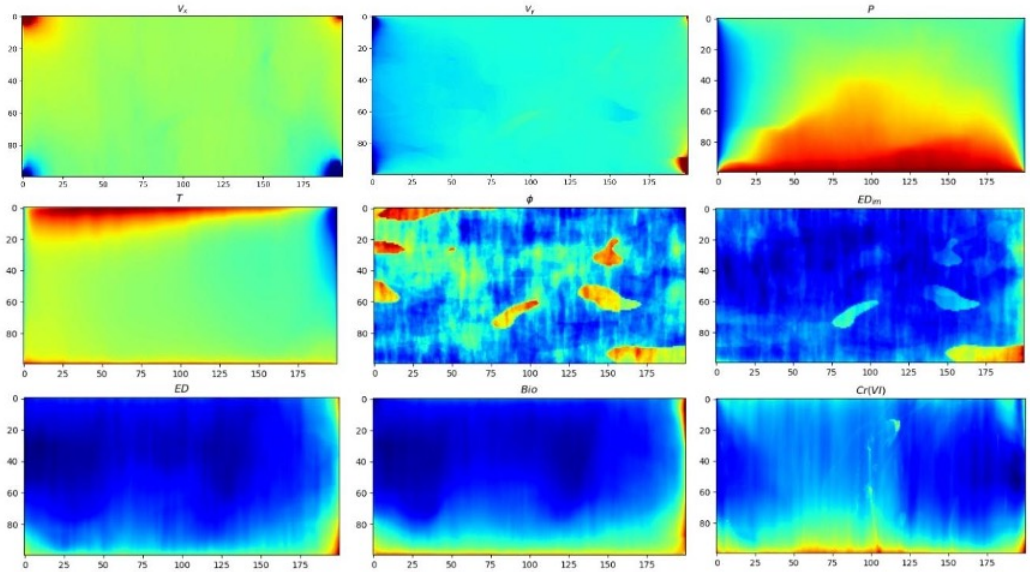

Figure 9: General (averaged over all simulations and time steps) trends for key physiochemical features. Each variable is normalized, with 0 (dark blue) corresponding to low values and 1 (dark red) corresponding to high values.

rate for the rest of the simulation (Figs. 10d and 10e). The first inflection point (at t = 18 days) corresponds to the time when biomass growth starts to dramatically increase. This also represents the point that ED and ED-immobile start to significantly decrease, Cr(VI) starts to increase, and porosity starts to decrease. We find that the relationship between biomass concentrations (in mol/m^3) and porosity can be described via the equation

$$\phi = .141 - 10^{-4} C_{bio} \tag{4}$$

where C_{bio} is the biomass concentration. This equation may be useful for predicting general trends in porosity as a function of biomass concentrations, although it is important to note that this function only represents our average simulation, and the exact value of this function will depend on a variety of factors such as soil type, microbial community structure, flow rates, and nutrient concentrations. At the highest amounts of growth (around day 46-52), biomass growth has a clear correspondence with pressure and V_x (Figs. 10b and 10a). The increase in pressure corresponds to a large decrease in the magnitude of V_x and a small increase in the magnitude of V_y. These

changes in flow then cause a an increase in molasses, chromium and the rate of biomass biomass growth. Around $t = 52$, the pressure starts to drop again and the magnitude of V_x increases, resulting in decreases in biomass growth, Cr(VI) and ED. At $t = 60$, the molasses concentrations and biomass growth rate start to increase again, but the chromium concentration continues to decrease. The vertical flow (V_x) thus seems to have a large effect due to the transport input conditions at the top boundary. Specifically, greater negative vertical velocities, representing flow from the top of the domain to the bottom, seem to result in a increase in molasses concentrations, which thus causes an increase in biomass growth. Although biomass growth and molasses concentrations are enhanced due to increased nutrient flux from the top boundary, the amount of Cr(VI) is also increased from the greater top-boundary flow, resulting in a small increase in Cr(VI) concentrations from day 42 to day 52. At $t = 70$, we approach the steady-state trends of the simulations. From this point onward, the magnitude of V_y slowly decreases, V_x and pressure slowly increase, biomass growth and Cr(VI) slowly decrease, and molasses slowly increases. At this point, biomass concentrations are relatively high, meaning the increase in V_x and pressure cause a corresponding decrease in growth due to velocity-based biomass decay. While at $t = 50$ the spike in V_x causes an increase in the biomass growth rate, by $t = 70$ it starts to cause a decrease in the growth rate. The greater negative values of V_x also should result in increased concentrations of Cr(VI) considering the transport boundary conditions. However, because ED concentrations steadily increase due to the decrease in biomass growth, the increased amount of abiotic reduction is enough to cause a decrease in Cr(VI). We can also see the dominance of abiotic reduction over biotic reduction through the beginning of the time series plots. From day 0 to day 16 there is an increase in ED of 0.1e-5 which corresponds to a decrease in Cr(VI) of about 0.2e-5. From day 80 to day 120 we observe a similar increase in ED concentration of 0.1e-5 which corresponds to a 0.1e-5 decrease in Cr(CI) concentration. Thus, the decrease in Cr(VI) concentration for the same relative increase in ED concentration is greater when there is little to no biomass, meaning abiotic reduction is the primary reason (besides transport boundary conditions) for the decreases in Cr(VI) in our simulations.

These findings reveal the intricate temporal dynamics of biomass growth, nutrient cycling, and chromium reduction in the HZ. The identification of key inflection points and the quantification of relationships between variables, such as biomass concentration and porosity, provide valuable insights for

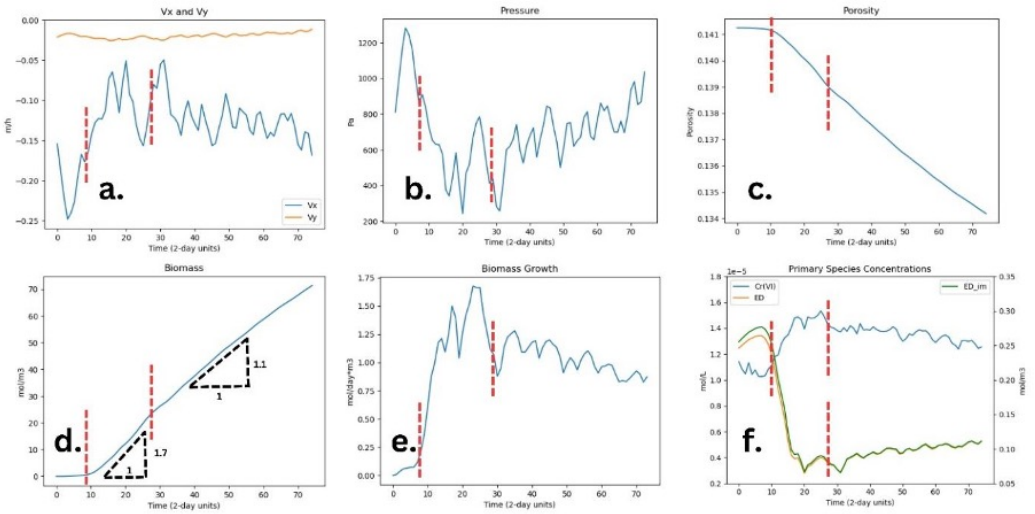

Figure 10: General (averaged over all simulations and spatial dimensions) time series for key physio-chemical features. The red dotted lines show the approximate time of the biomass growth inflection points. (a) V_x (blue) and V_y (orange). (b) Pressure. (c) Porosity. (d) Biomass. (e) Biomass growth. (f) Cr(VI) (blue), ED (orange), and ED-immobile (green). Here, biomass growth is shown to primarily be dependent on ED concentration. The Cr(VI) timeseries shows an increase in concentration as molasses decreases, indicating the dominance of abiotic reduction over biotic reduction.

predicting system behavior and optimizing remediation efforts.

3.3. Sensitivity Analysis of Biomass Growth

To gain deeper insights into the abiotic determinants of biomass growth in the hyporheic zone, we used sensitivity and correlation analysis. The sensitivity analysis (Fig. 11) shows the biomass time series and spatial distributions of the last time step for 6 equally spaced values of a simulation input variable (keeping all other input variables constant). We performed sensitivity analysis for five key variables (temperature, carbon reuse efficiency, homogeneous permeability value, V_x, and the biomass crowding parameter). The temperature sensitivity analysis (Fig. 11a) shows that at higher temperatures the biomass growth rate increases, leading to differences in biomass concentrations that remain constant after about day 60. The spatial distributions show more variation in biomass concentrations for higher-temperature simulations. The carbon reuse efficiency (D), is a Chrotran parameter that defines the stoichiometric relationship between the ED and biomass. So for D = 1, one mol of ED creates one mol of biomass. The sensitivity analysis for D (Fig. 11b)

shows that lower values of D result in an increase in biomass growth that increases over time. The spatial distributions show that for lower values of D, the biomass is able to spread further throughout the domain. The permeability sensitivity analysis (Fig. 11c) indicates that mean permeability of the domain has a huge impact on biomass growth. For $k = 1 \times 10^{-}12$ there is a minute amount of biomass growth that can be observed in the bottom corners of the spatial distribution, but for lower permeability values, we don't observe any biomass growth. A permeability of $1 \times 10^{-}12\ m^2$ is representative of silty sand or permeable basalt (cite), implying that aquifers primarily composed of these materials (or lower-permeability materials) are not likely to house large concentrations of biomass. The V_x sensitivity analysis (Fig. 11d) indicates that greater vertical velocity contributes to a more sigmoidal (as opposed to linear or exponential) growth curve, results in generally greater biomass growth, and causes the growth curve to have small undulations. This wave-like behavior is a result of spikes in flow speed causing significant shearing of biomass, thus briefly decreasing the rate of biomass growth. α is another Chrotran parameter that describes biomass crowding. For higher values of alpha, we see slightly lower biomass concentrations over time, although the main difference is in the spatial distributions (Fig. 11e). When crowding is high (low alpha), we get much higher concentrations of biomass that are constrained to the first few centimeters of the domain. When crowding is low, we get a lower maximum biomass concentration, but the biomass is spread throughout the entire domain. Overall, the sensitivity analysis shows that many input features result in large changes to biomass concentrations, illustrating the general complexity of determining the most important impacts on biomass.

To further investigate the impacts of our simulation variables on biomass concentrations in a more general sense, we used PCA and cluster analysis (Fig. 12a) to identify groupings and large-scale relationships across all of our simulations. The first principle component seems to be primarily determined by V_x, temperature, ED, and P, meaning it largely represents the flow and transport boundary conditions. The second principle component is determined by biomass and porosity, which indicates that it represents both the boundary conditions, and the biomass growth conditions. Porosity is the only variable in the PCA that isn't significantly influenced by the boundary conditions, which further reinforces our interpretation of the principle components. We also see interesting sets of groups that form as a result of cluster analysis in the space of the first two principle components. The top

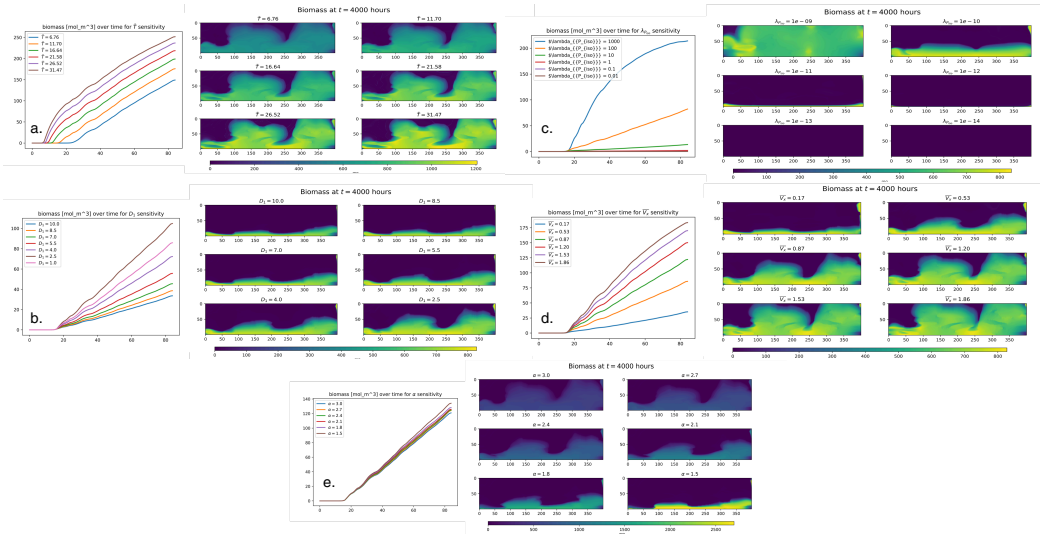

Figure 11: Sensitivity analysis for selected features with large impacts on biomass growth. For each feature, we show the time series, as well as the spatial distributions of biomass for the final time step. The colorbars show biomass concentration in mol/m3. (a) Temperature sensitivity. (b) Carbon reuse efficiency sensitivity. (c) Biomass crowding sensitivity. (d) Vx sensitivity.

right can be described as the biomass cluster, the top left is the temperature cluster, the bottom left is the Cr(VI) cluster, the middle is the standard deviation and V_y cluster, and the bottom right is the ED/P cluster. These clusters represent most of the strongest relationships with biomass concentrations in our simulations (Fig. 12b). Specifically, the strongest correlations for biomass with other physio-chemical variables are σ_P (.37), $\sigma_{ED_{im}}$ (.36), pressure (.32), σ_{V_x} (.31), σ_{V_y} (.31), σ_{ED} (.31), ED (.30), ED_{im} (.30), σ_T (-.21), then chromium (-.18). Surprisingly, biomass is more strongly correlated with the standard deviation of features than the features themselves (except for chromium). The reason for this is likely because the standard deviations of features are more strongly correlated with the simulation boundary conditions (as denoted by SIM_{ID}) than the feautures are (Fig. 12b).

The PCA also indicates a significant amount of correlation between ED, ED_{im}, P, σ_P, σ_{V_x}, σ_{V_y}, and $\sigma_{ED_{im}}$, which are all anticorrelated with T, Vx, and σ_T. This is partially due to the fact that the simulations where the flow was from the river to the groundwater (i.e., losing streams) had the largest maximum vertical velocities and highest temperatures. Similarly, the gaining

streams had higher nutrient concentrations, so this grouping likely represents the gaining streams. However, higher pressure is not necessarily correlated with the gaining simulations. Instead, P likely occupies this position in the 2D PCA space because of its high correlation with ED. An increase in pressure causes an increase in the magnitude of V_x or V_y, which almost always causes an increase in ED concentrations as more nutrients enter the domain.

The correlations indicated in the PCA are slightly different from those of the correlation matrix, both because the PCA doesn't explicitly represent correlations, and because the PCA was only calculated with physio-chemical features, but the correlation matrix also includes the biomass growth parameters from Chrotran (λ_a, λ_b, λ_c, and λ_d), permeability covariance ratio, max length in the permeability covariance ratio, time, and Sim_{ID}. For example, the PCA shows a slight amount of positive correlation between biomass and this ED/P grouping, although it is most strongly positively correlated with the standard deviations of biomass and ED. However, σ_{ED} is in a different cluster than biomass, indicating some strong differences in the first priciple component between biomass and σ_{ED}. Also, temperature and biomass are slightly negatively correlated in the PCA, but are slightly positively correlated in the correlation matrix. The most general correlations are given by the correlation matrix because more variables were used to compute them.

Thus, we use the correlation matrix (and specifically any correlations with magnitude greater than 0.12) as the basis to alter our feedback cycles figure. To portray the fact that this new feedback cycle (Fig. 13) purely represents our simulations, we have removed oxygen from the cycle and added Cr(VI). Also, to indicate the difference between speed and flow direction, we have added pressure to the cycle, and changed "flow vector" to V_x. The new correlation matrix shows temperature to be negatively correlated with the flow vector, and since correlations don't allow for two-way causative analysis, there is only a positive correlation between biomass and ED (no negative correlation).

This comprehensive sensitivity analysis reveals the relative importance of various factors influencing biomass growth in the HZ. The identification of permeability as a critical factor and the complex relationships between flow conditions, nutrient availability, and biomass distribution provide essential insights for designing effective bioremediation strategies and improving predictive models of HZ processes.

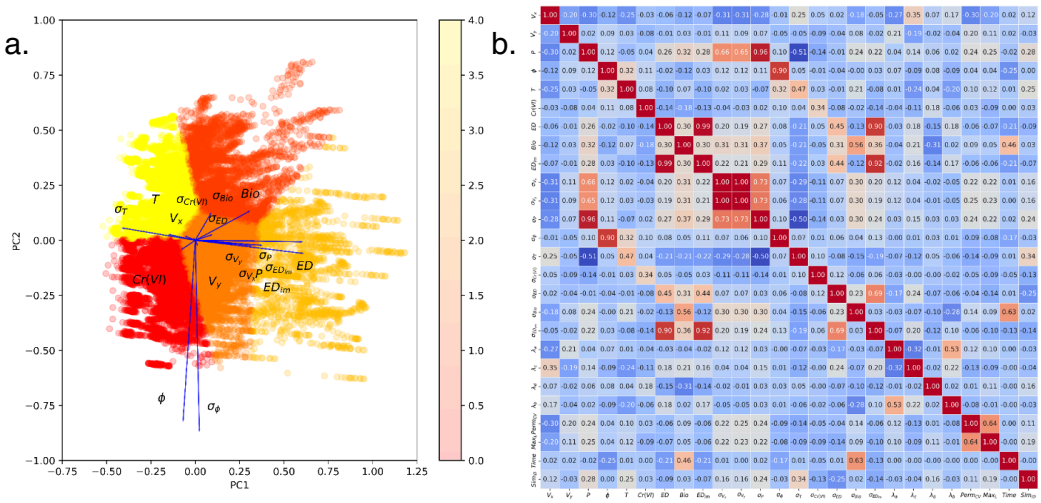

Figure 12: PCA for physio-chemical features that were varied for each simulation. The x-axis shows the first principal component, the y-axis shows the second principal component, and the color bar represents the KMeans clustering output in the 2D PCA space. ED, although the largest correlations for biomass are with σ_{Bio} and σ_{ED}. Cr(VI) shows complete anticorrelation with biomass, which is somewhat surprising given our other results that show the dominance of abiotic reduction over biotic reduction (Fig. 3). σ_ϕ and ϕ aren't strongly correlated with anything, although the show slight positive correlation with Cr(VI) and negative correlation with biomass, indicating that higher porosity soils may have less reductive capacity.

3.4. Velocity-Based Biomass Decay Sensitivity Analysis

In addition to using sensitivity analysis to understand the relationships between the variables of our simulations, we also use sensitivity analysis to illustrate the impact of changing the parameters of our velocity-based biomass decay equation. Specifically, we show the spatial distributions at t=5400 hours for biomass (Figs. 14a-13f) and Cr(VI) (Figs. 14g-13l) for the situations of the calibrated decay parameters, no decay, high β, low β, high α, and low α. The spatial distributions for biomass generally show that biomass concentrations, as well as the spatial extent of the biomass plume, are highly dependent on the velocity-based biomass decay parameters. The simulation with no decay has the highest concentrations of biomass, followed by the $\beta = 1.2$ simulation, then the $\alpha = 2 \times 10^{-4}$ simulation. The $\alpha = 2 \times 10^{-10}$ simulation shows essentially no difference from the calibrated simulation, and the $\beta = 0.4$ simulation shows much lower concentrations than the calibrated simulation. For the case of no decay, the spatial distributions aren't very

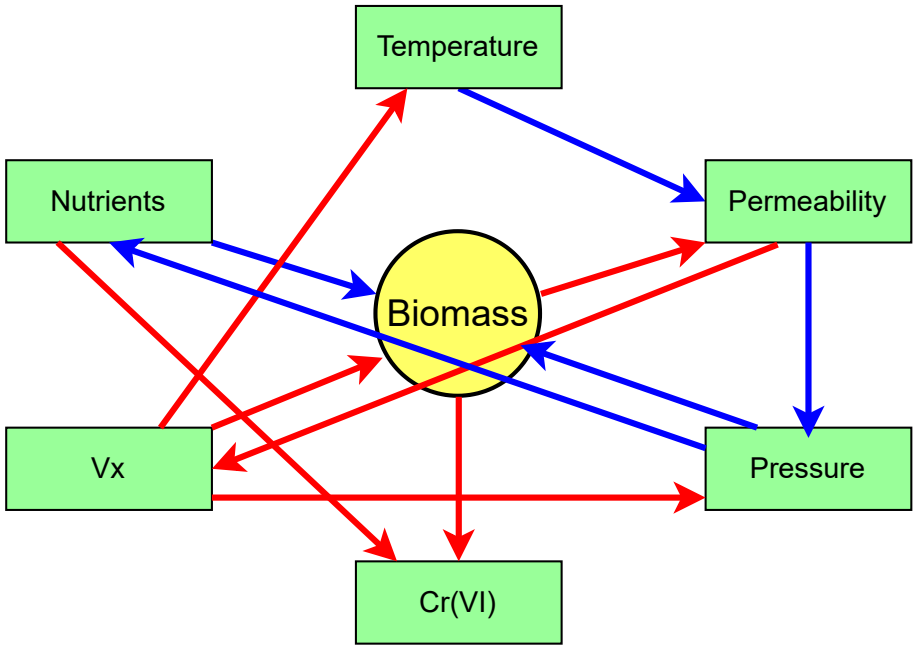

Figure 13: Biomass feedback v2.

different from those of the calibrated decay, but the low beta case has a dramatically different spatial distribution. The Cr(VI) distributions follow the same patterns as the biomass, except the no decay, $\alpha = 2 \times 10^{-4}$ and $\beta = 1.2$ simulations show less chromium (or more Cr(VI) reduction) than the other simulations.

We also show the spatial distributions of porosity (Fig. 14m) and V_x (Fig. 14n) to gain deeper insight into the spatial distributions of biomass and Cr(VI). The spatial distribution of biomass for the calibrated decay parameters (Fig. 14a) are largely determined by the low-porosity area at x=250, y=50 and the high porosity zone at x=175, y=80. Decay is highest where fluid speed is highest, which is in the corners of the simulation and the low-porosity zones in the middle and left side of the domain (Fig. 14n). Unsurprisingly, these are the areas where we see the greatest amount of difference from the simulation with calibrated parameters. Specifically, the no decay (Fig. 14b) and $\beta = 1.2$ (Fig. 14e) simulations for biomass show

much greater biomass concentrations in the corners and middle high-porosity area of the domain compared to that of the calibrated decay simulation.

Surprisingly, although our general results (Fig. 10) show increased biomass results in a relative decrease Cr(VI) reduction, we observe the opposite trend here. Looking at the time series outputs for the sensitivity analysis can help clear this confusion (Fig. 15). For biomass (Fig. 15a) and chromium (Fig. 15b), the time series plots show the relative differences highlighted by the spatial distribution plots. The time series plots for molasses (Fig. 15c), on the other hand, shows very little difference due to changes in the velocity-based biomass decay parameters. Thus, we see that for each case of different parameter values, the same amount of molasses is consumed by biomass (besides the case of $\beta = 0.4$). Thus, greater biomass concentrations result in greater chromium reduction, since each simulation has a relatively equal amount of abiotic reduction. In other words, the increases/decreases in bioreduction due to parameter changes in the velocity-based biomass decay equation don't result in large decreases/increases in abiotic reduction.

This sensitivity analysis of the novel velocity-based biomass decay model demonstrates its significant impact on biomass distribution and chromium reduction. The results highlight the importance of accurately representing biofilm dynamics in response to hydrodynamic conditions, which can substantially influence the overall effectiveness of bioremediation processes in the HZ.

4. Conclusions

This study provides valuable insights into the complex dynamics of biomass growth and chromium reduction in the hyporheic zone. Through a series of sophisticated simulations and comprehensive analyses, we have demonstrated the intricate interplay between various physio-chemical features, including flow characteristics, nutrient concentrations, temperature, and permeability. Our novel velocity-based biomass decay model, incorporated into PFLOTRAN, offers a more nuanced representation of biofilm dynamics in response to hydrodynamic conditions. This advancement allows for more accurate predictions of biomass distribution and its impact on contaminant reduction processes. Key findings from this study include:

- The identification of abiotic reduction as the dominant process in chromium remediation, even in scenarios with high biomass concentrations.

- The quantification of relationships between biomass concentration and porosity, providing a useful predictive tool for future modeling efforts.
- The revelation of complex feedback mechanisms between flow conditions, nutrient availability, and biomass growth, highlighting the importance of considering spatial heterogeneity in hyporheic zone modeling.
- The demonstration of the significant impact of velocity-based biomass decay on overall system behavior and contaminant reduction efficiency.

These results have far-reaching implications for bioremediation strategies in contaminated aquifers. By providing a more accurate representation of biomass dynamics and contaminant reduction processes, this study enables better prediction and optimization of remediation efforts.

Future research should focus on validating these findings with field studies and exploring the implications for bioremediation strategies in diverse hyporheic zone environments. Additionally, the integration of this advanced biomass decay model with other reactive transport processes could further improve our understanding and prediction of complex subsurface biogeochemical dynamics.

References

[1] T. Singh, L. Wu, J. D. Gomez-Velez, J. Lewandowski, D. M. Hannah, S. Krause, Dynamic hyporheic zones: Exploring the role of peak flow events on bedform-induced hyporheic exchange, Water Resources Research 55 (1) (2019) 218–235.

[2] M. H. Kaufman, M. B. Cardenas, J. Buttles, A. J. Kessler, P. L. Cook, Hyporheic hot moments: Dissolved oxygen dynamics in the hyporheic zone in response to surface flow perturbations, Water Resources Research 53 (8) (2017) 6642–6662.

[3] F. Boano, J. W. Harvey, A. Marion, A. I. Packman, R. Revelli, L. Ridolfi, A. Wörman, Hyporheic flow and transport processes: Mechanisms, models, and biogeochemical implications, Reviews of geophysics 52 (4) (2014) 603–679.

[4] L. Bardini, F. Boano, M. Cardenas, R. Revelli, L. Ridolfi, Nutrient cycling in bedform induced hyporheic zones, Geochimica et Cosmochimica Acta 84 (2012) 47–61.

[5] A. J. Boulton, S. Findlay, P. Marmonier, E. H. Stanley, H. M. Valett, The functional significance of the hyporheic zone in streams and rivers, Annual review of ecology and systematics 29 (1) (1998) 59–81.

[6] J. V. Kunz, M. D. Annable, J. Cho, W. von Tümpling, K. Hatfield, S. Rao, D. Borchardt, M. Rode, Quantifying nutrient fluxes with a new hyporheic passive flux meter (hpfm), Biogeosciences 14 (3) (2017) 631–649.

[7] S. Roy Chowdhury, J. P. Zarnetske, M. S. Phanikumar, M. A. Briggs, F. D. Day-Lewis, K. Singha, Formation criteria for hyporheic anoxic microzones: Assessing interactions of hydraulics, nutrients, and biofilms, Water Resources Research 56 (3) (2020) no–no.

[8] S. Cook, O. Price, A. King, C. Finnegan, R. van Egmond, H. Schäfer, J. M. Pearson, S. Abolfathi, G. D. Bending, Bedform characteristics and biofilm community development interact to modify hyporheic exchange, Science of the Total Environment 749 (2020) 141397.

[9] A. Caruso, F. Boano, L. Ridolfi, D. L. Chopp, A. Packman, Biofilm-induced bioclogging produces sharp interfaces in hyporheic flow, redox conditions, and microbial community structure, Geophysical Research Letters 44 (10) (2017) 4917–4925.

[10] X. Ping, M. Jin, Y. Xian, Effect of bioclogging on the nitrate source and sink function of a hyporheic zone, Journal of Hydrology 590 (2020) 125425.

[11] L. Wang, Z. Wang, Y. Li, W. Cai, Y. Zou, C. Hui, Deciphering solute transport, microbiota assembly patterns and metabolic functions in the hyporheic zone of an effluent-dominated river, Water Research 251 (2024) 121190.

[12] Y. Wang, Y. Wang, J. Shang, L. Wang, Y. Li, Z. Wang, Y. Zou, W. Cai, L. Wang, Redox gradients drive microbial community assembly patterns and molecular ecological networks in the hyporheic zone of effluent-dominated rivers, Water Research 248 (2024) 120900.

[13] D. Liang, J. Song, J. Xia, J. Chang, F. Kong, H. Sun, D. Cheng, Y. Zhang, et al., Effects of heavy metals and hyporheic exchange on microbial community structure and functions in hyporheic zone, Journal of Environmental Management 303 (2022) 114201.

[14] L. Zhang, C. Zhang, K. Lian, C. Liu, Effects of chronic exposure of antibiotics on microbial community structure and functions in hyporheic zone sediments, Journal of Hazardous Materials 416 (2021) 126141.

[15] Y. Xian, M. Jin, H. Zhan, X. Liang, Permeable biofilms can support persistent hyporheic anoxic microzones, Geophysical Research Letters 49 (14) (2022) e2021GL096948.

[16] F. Kazemifar, G. Blois, M. Aybar, P. Perez Calleja, R. Nerenberg, S. Sinha, R. J. Hardy, J. Best, G. H. Sambrook Smith, K. T. Christensen, The effect of biofilms on turbulent flow over permeable beds, Water Resources Research 57 (2) (2021) e2019WR026032.

[17] G. Wei, J. Q. Yang, Impacts of hydrodynamic conditions and microscale surface roughness on the critical shear stress to develop and thickness of early-stage pseudomonas putida biofilms, Biotechnology and bioengineering 120 (7) (2023) 1797–1808.

[18] E. Tsagkari, S. Connelly, Z. Liu, A. McBride, W. T. Sloan, The role of shear dynamics in biofilm formation, npj Biofilms and Microbiomes 8 (1) (2022) 33.

[19] N. S. Panikov, Microbial growth kinetics (1995).

[20] T. D. Brock, Microbial growth rates in nature, Bacteriological reviews 35 (1) (1971) 39–58.

[21] P. Gikas, S. Sengor, T. Ginn, J. Moberly, B. Peyton, The effects of heavy metals and temperature on microbial growth and lag, Global Nest J 11 (3) (2009) 325–32.

[22] M. Peleg, A new look at models of the combined effect of temperature, ph, water activity, or other factors on microbial growth rate, Food Engineering Reviews 14 (1) (2022) 31–44.

[23] Y. Zhang, Q. Tang, P. Shi, T. Katsumi, Influence of bio-clogging on permeability characteristics of soil, Geotextiles and Geomembranes 49 (3) (2021) 707–721.

[24] L. Allison, Effect of microorganisms on permeability of soil under prolonged submergence, Soil Science 63 (6) (1947) 439–450.

[25] C. I. Steefel, S. Molins, Crunchflow, Software for modeling multicomponent reactive flow and transport. User's manual (2009) 12–91.

[26] P. C. Lichtner, G. E. Hammond, C. Lu, S. Karra, G. Bisht, B. Andre, R. Mills, J. Kumar, Pflotran user manual: A massively parallel reactive flow and transport model for describing surface and subsurface processes, Tech. rep., Los Alamos National Laboratory (LANL), Los Alamos, NM (United States ... (2015).

[27] M. D. White, M. Oostrom, Stomp subsurface transport over multiple phases version 3.0 user's guide, Tech. rep., Pacific Northwest National Lab., Richland, WA (US) (2003).

[28] Z. Hou, H. Ren, C. J. Murray, X. Song, Y. Fang, E. V. Arntzen, X. Chen, J. C. Stegen, M. Huang, J. D. Gomez-Velez, et al., A novel construct for scaling groundwater–river interactions based on machine-guided hydromorphic classification, Environmental Research Letters 16 (10) (2021) 104016.

[29] D. Dwivedi, I. C. Steefel, B. Arora, G. Bisht, Impact of intra-meander hyporheic flow on nitrogen cycling, Procedia Earth and Planetary Science 17 (2017) 404–407.

[30] S. B. Yabusaki, Y. Fang, K. H. Williams, C. J. Murray, A. L. Ward, R. D. Dayvault, S. R. Waichler, D. R. Newcomer, F. A. Spane, P. E. Long, Variably saturated flow and multicomponent biogeochemical reactive transport modeling of a uranium bioremediation field experiment, Journal of contaminant hydrology 126 (3-4) (2011) 271–290.

[31] Y. Fang, X. Chen, J. Gomez Velez, X. Zhang, Z. Duan, G. E. Hammond, A. E. Goldman, V. A. Garayburu-Caruso, E. B. Graham, A multirate mass transfer model to represent the interaction of multicomponent biogeochemical processes between surface water and hyporheic zones (swat-mrmt-r 1.0), Geoscientific Model Development 13 (8) (2020) 3553–3569.

[32] S. K. Hansen, S. Pandey, S. Karra, V. V. Vesselinov, Chrotran 1.0: A mathematical and computational model for in situ heavy metal remediation in heterogeneous aquifers, Geoscientific Model Development 10 (12) (2017) 4525–4538.

[33] K. Chen, X. Chen, J. C. Stegen, J. A. Villa, G. Bohrer, X. Song, K.-Y. Chang, M. Kaufman, X. Liang, Z. Guo, et al., Vertical hydrologic exchange flows control methane emissions from riverbed sediments, Environmental Science & Technology 57 (9) (2023) 4014–4026.

[34] H. Le Lay, Z. Thomas, F. Rouault, P. Pichelin, F. Moatar, Characterization of diffuse groundwater inflows into stream water (part ii: quantifying groundwater inflows by coupling fo-dts and vertical flow velocities), Water 11 (12) (2019) 2430.

[35] J. Ren, B. Chen, W. Zhang, L. Men, J. Yang, Y. Li, Quantification of the temporal–spatial distributions characteristics of streambed hyporheic exchange fluxes with the seasonal variation using heat as a tracer, Environmental Earth Sciences 79 (2020) 1–19.

[36] Z. Wang, M. Zhao, Z. Yan, Y. Yang, K. J. Niklas, H. Huang, T. D. Mipam, X. He, H. Hu, S. J. Wright, Global patterns and predictors of soil microbial biomass carbon, nitrogen, and phosphorus in terrestrial ecosystems, Catena 211 (2022) 106037.

[37] A. Golparvar, Y. Zhou, K. Wu, J. Ma, Z. Yu, A comprehensive review of pore scale modeling methodologies for multiphase flow in porous media, Advances in Geo-Energy Research 2 (4) (2018) 418–440.

[38] H. Jasak, A. Jemcov, Z. Tukovic, et al., Openfoam: A c++ library for complex physics simulations, in: International workshop on coupled methods in numerical dynamics, Vol. 1000, Dubrovnik, Croatia), 2007, pp. 1–20.

[39] H. G. Weller, G. Tabor, H. Jasak, C. Fureby, A tensorial approach to computational continuum mechanics using object-oriented techniques, Computers in physics 12 (6) (1998) 620–631.

[40] D. S. Esser, J. H. Leveau, K. M. Meyer, Modeling microbial growth and dynamics, Applied microbiology and biotechnology 99 (2015) 8831–8846.

[41] C. Cruz-Paredes, D. Tájmel, J. Rousk, Can moisture affect temperature dependences of microbial growth and respiration?, Soil Biology and Biochemistry 156 (2021) 108223.

[42] A. T. Nottingham, E. Bååth, S. Reischke, N. Salinas, P. Meir, Adaptation of soil microbial growth to temperature: using a tropical elevation gradient to predict future changes, Global change biology 25 (3) (2019) 827–838.

[43] K.-Y. LI, J. A. TORRES, Microbial growth estimation in liquid media exposed to temperature fluctuations, Journal of food science 58 (3) (1993) 644–648.

[44] D. A. Ratkowsky, J. Olley, T. McMeekin, A. Ball, Relationship between temperature and growth rate of bacterial cultures, Journal of bacteriology 149 (1) (1982) 1–5.

[45] S. P. Hendricks, Microbial ecology of the hyporheic zone: a perspective integrating hydrology and biology, Journal of the North American Benthological Society 12 (1) (1993) 70–78.

[46] M. E. Newcomer, S. S. Hubbard, J. H. Fleckenstein, U. Maier, C. Schmidt, M. Thullner, C. Ulrich, N. Flipo, Y. Rubin, Influence of hydrological perturbations and riverbed sediment characteristics on hyporheic zone respiration of co2 and n2, Journal of Geophysical Research: Biogeosciences 123 (3) (2018) 902–922.

[47] M. Azizi-Rad, G. Guggenberger, Y. Ma, C. A. Sierra, Sensitivity of soil respiration rate with respect to temperature, moisture and oxygen under freezing and thawing, Soil Biology and Biochemistry 165 (2022) 108488.

[48] H. Monterroso, M. A. Widdowson, W. S. Lotts, K. B. Strom, E. T. Hester, Effects of boundary hydraulics, dissolved oxygen, and dissolved organic carbon on growth and death dynamics of aerobic microbes in riverbed dune-induced hyporheic zones, Science of the Total Environment 906 (2024) 167401.

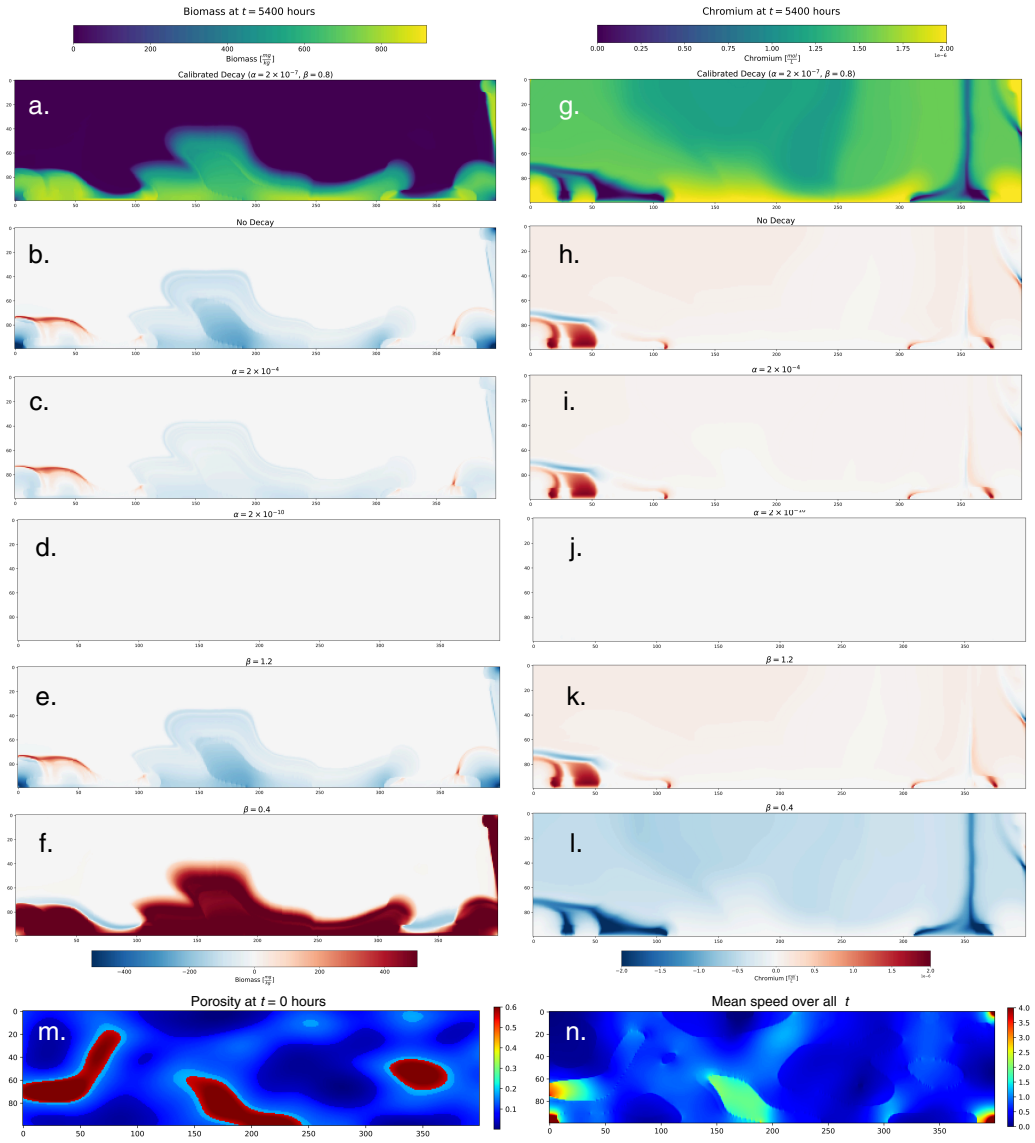

Figure 14: Spatial distributions of biomass (a-f) and chromium (g-l) at $t = 5400$ hours for the calibrated decay values (a & g), no decay (b & h), $\alpha = 2 \times 10^{-4}$ (c & i), $\alpha = 2 \times 10^{-10}$ (d & j), $\beta = 1.2$ (e & k), and $\beta = 0.4$ (f & l). Spatial distributions of porosity at $t = 0$ (m) and V_x averaged over all t (n) are used to further understand the differences in simulation output due to changes in the velocity-based biomass decay parameters. The top colormaps represents the concentrations shown in the calibrated decay plots (a & g), and the bottom colormaps represent the feature (biomass or chromium) concentration of the calibrated decay minus the feature concentration for the particular change in parameter value.

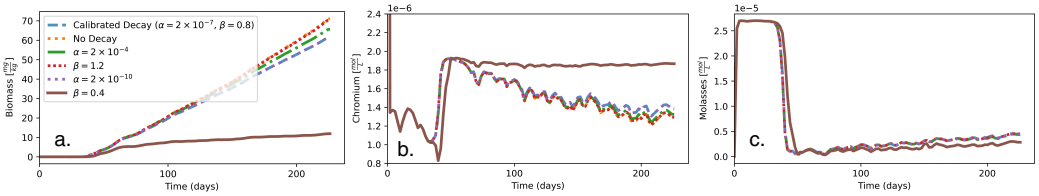

Figure 15: Time series plots (averaged over both spatial dimensions) for biomass (a), chromium (b), and molasses (c) for simulations with the calibrated decay parameters ($\alpha = 2 \times 10^{-7}$, $\beta = 0.8$), no decay, $\alpha = 2 \times 10^{-7}$, $\alpha = 2 \times 10^{-10}$, $\beta = 1.2$, and $\beta = 0.4$. Differences due to parameter changes are relatively small except for $\beta = 0.4$, and are largest for biomass, then chromium, then molasses.